19th International Conference on
Adaptive Structures and Technologies
October 6-9, 2008
Ascona, Switzerland

Macro-Fiber Composite Actuated Thin Clamped-Free Benders and Thin Simply-Supported Morphing Airfoils

Onur Bilgen[1*], Alper Erturk[2], Daniel J. Inman[1], and Kevin B. Kochersberger[1]

Center for Intelligent Material Systems and Structures
Virginia Polytechnic Institute and State University, Blacksburg, VA 24061, USA
[1] Department of Mechanical Engineering
[2] Department of Engineering Science and Mechanics
* Corresponding author: E-mail: onurb@vt.edu
310 Durham Hall, Blacksburg, VA 24061, USA
Phone: +1 (540) 231- 2902; Fax: +1 (540) 231-2903

ABSTRACT

A type of piezoceramic composite actuator commonly known as Macro-Fiber Composite (MFC) is used for actuation in a variable camber airfoil design. First, a distributed parameter electromechanical model is proposed to predict the structural response to voltage actuation of clamped-free thin cantilevered beams. The structural frequency response behavior is investigated experimentally for cantilevered unimorph MFC actuated benders with aluminum, brass and steel substrate materials of different thicknesses. Second, the study focuses on actuation modeling and response characterization under aerodynamic loads for flat plate airfoils with variable pinned boundary conditions. Thin unimorph/bimorph benders are pinned in two variable locations along the chordwise direction. Two extreme examples are: 1) Airfoil pinned at its leading edge and at its trailing edge; 2) A clamped-free airfoil. Any combination in between the two extremes is also evaluated for geometric and aerodynamic response. Finally, wind tunnel experiments are conducted on a 1.2% thick, 127 mm chord MFC actuated bimorph airfoil.

Keywords: Variable camber airfoil, morphing wing, unimorph actuator, MFC

1. INTRODUCTION

The past few decades have seen the development and integration of active materials into a variety of host structures as a superior means of measuring and controlling its behavior. [1] Piezoceramics remain the most widely used “smart” or active material because they offer high actuation authority and sensing over a wide range of frequencies. Specifically, piezoceramic materials have been extensively studied and employed in aerospace structures by performing shape and flow control. Macro-Fiber Composite (MFC) is a type of piezoceramic material that offers structural flexibility and high actuation authority. A common disadvantage with piezoceramic actuators and with the MFC actuator is that they require high voltage input. An MFC actuator could require up to 1.8 kV and some active materials may require up to 10 kV. In contrast, the current drain is usually low creating reasonable power consumption. The high voltage demand requires additional amplifiers and electronic circuits to be included in the system. Due to the weight of the electronic logistical systems that come along with the active material, these actuators have been used mostly in large vehicles or in the laboratory environment. With the continuing development in the electronic systems, active materials become feasible in small platforms such as MAVs.

Smart materials can be employed for control in thin, composite-wing MAVs. There are several benefits of using camber control via solid-state active materials over the trailing edge control using conventional control surfaces. First, the low Reynolds Number flow regime can result in flow separation that reduces the effectiveness of a trailing edge control surface. Second, power-limited aircraft such as MAVs cannot afford to lose energy through control surface drag. Finally, the opportunity for flow control is inherent in the active material due to its direct effect on circulation and high operating bandwidth.

Recently, Bilgen, et. al. [2,3] presented a new application for piezo-composite actuators on a 0.76 meter wingspan morphing wing air vehicle. In this application, two MFC patches are bonded to the wings of a small demonstration vehicle, and the camber of the wing is changed with actuator voltage. This morphing control directly affects the circulation by changing the wing’s camber, and adequate control authority is demonstrated in the wind tunnel as well as in flight. The aircraft demonstrates that lightweight, conformal

actuators can be used as primary control surfaces on an aircraft. All electronics are powered by an 11.1 V Lithium-Polymer battery, a common choice for remotely controlled aircraft.

The weight benefit and bandwidth of a smart material actuator makes it ideal for smaller aircraft applications. In addition to replacing conventional control surfaces, these actuators can be effective in dynamic laminar separation bubble (LSB) control and any application where flow vectoring is desired. For thrust vectoring, the challenge is found in operating a relatively compliant, thin structure (desirable for piezo-ceramic actuators) at high dynamic pressures to extract controlling forces. Establishing boundary conditions that are stiff enough to prevent flutter and departure, but compliant enough to allow the range of available motion is the central challenge in developing a morphing wing. Novel methods of supporting the actuator can take advantage of aerodynamic loads to reduce control input moments and increase control effectiveness.

Static flow deflections and lift generation are obvious applications of a morphing airfoil, but the bandwidth advantage of a conformal actuator also opens the possibility for dynamic actuation that may have significant advantages. Bilgen et. al.[4] recently presented static flow vectoring via MFC actuated thin airfoils. Therein, wind tunnel experiments and theoretical analysis are conducted on a 1.15% thick, 54 mm chord, and 108 mm span fiberglass/epoxy composite airfoil. Wind tunnel results and analytical evaluation of the airfoils showed comparable effectiveness to conventional actuation systems. Deformation of the airfoils due to pressure distribution is studied by a finite element method. All concepts presented adequate stiffness for flow speeds up to 30 m/s.

This paper extends the authors' previous work by modeling and experimentally evaluating thin morphing airfoils. First, analytical electromechanical model of an MFC actuated thin clamped-free beam is presented. The model prediction of the tip velocity frequency response function is compared to the experimental values. Next, concepts for thin airfoils with variable pinned boundary conditions are introduced. The airfoils are theoretically evaluated for lift and drag performance at different flow velocities. Finally, a prototype airfoil is presented and wind tunnel results are discussed. The paper concludes with a brief discussion of the results and the authors' future research in the area.

2. AN ELECTROMECHANICAL MODEL FOR MFC ACTUATED CLAMPED BEAMS

2.1. Electromechanical Model for Transverse Vibration Response

Macro-Fiber Composites are developed at NASA Langley Research Center.[5] An MFC is a layered, planar actuation device that employs rectangular cross-section, unidirectional piezoceramic fibers embedded in a thermosetting polymer matrix. This active, fiber reinforced layer is then sandwiched between copper-clad Kapton film layers that have an etched interdigitated electrode pattern. A comprehensive manufacturing manual for MFC can be found in High and Wilkie. [6] The in-plane poling and subsequent voltage actuation allows the MFC to utilize the d_{33} piezoelectric effect, which is much stronger than the d_{31} effect used by traditional PZT actuators with through-the-thickness poling.[7] In order to predict the transverse vibration response of a cantilevered MFC unimorph due to a dynamic voltage excitation, a distributed parameter formulation is employed here.[8] Since the interdigitated electrodes have negligible thickness and the beam is fairly thin, the unimorph cantilever is modeled as a uniform Euler-Bernoulli beam. The MFCs studied here operate in the d_{33} mode of piezoelectricity and the respective (well-known) constitutive relation is

$$T_3 = c_{33}^E S_3 - e_{33} E_3 \tag{1}$$

where T_3 is the stress component, S_3 is the strain component, E_3 is the electric field component, e_{33} is the piezoelectric constant and c_{33}^E is elastic stiffness component at constant electric field (reduced for the thin beam theory).

Undamped free vibrations of the beam are governed by

$$\frac{\partial^2 M(x,t)}{\partial x^2} + c_s I \frac{\partial^5 w(x,t)}{\partial x^4 \partial t} + c_a \frac{\partial w(x,t)}{\partial t} + m \frac{\partial^2 w(x,t)}{\partial t^2} = 0 \tag{2}$$

where $M(x,t)$ is the internal bending moment (excluding the strain rate effect), $w(x,t)$ is the transverse deflection, $c_s I$ is the strain-rate damping term, c_a is the viscous damping coefficient and m is the mass per unit length of the beam. After expressing the strain component in terms of the curvature and the electric field in terms of the voltage ($E_3(t) = -v(t)/\Delta_{el}$ where $v(t)$ is the voltage across the interdigitated electrodes

and Δ_{el} is the effective electrode spacing) one can integrate the moment of Equation (1) and substitute in Equation (2) to obtain the coupled equation for the forced vibrations of the beam:

$$YI\frac{\partial^4 w(x,t)}{\partial x^4}+c_s I\frac{\partial^5 w(x,t)}{\partial x^4\partial t}+c_a\frac{\partial w(x,t)}{\partial t}+m\frac{\partial^2 w(x,t)}{\partial t^2}=-v(t)\frac{d^2\Gamma(x)}{dx^2} \tag{3}$$

where *YI* is the bending stiffness (obtained from the transformed cross-section) and $\Gamma(x)$ accounts for the spatial distribution of the electric potential [9]:

$$\Gamma(x)=\vartheta\sum_{i=1}^{N_e}\left\{\left(1+\frac{x-x_{i0}}{x_{i0}-x_{i1}}\right)\left[H\left(x-x_{i0}\right)-H\left(x-x_{i1}\right)\right]+\left(\frac{x-x_{i2}}{x_{i3}-x_{i2}}\right)\left[H\left(x-x_{i2}\right)-H\left(x-x_{i3}\right)\right]\right\} \tag{4}$$

where N_e is the number of electrode pairs over the beam length ($N_e \cong L_{act}/2\left(u_e+u_0\right)$ where L_{act} is the active beam length, u_e is the width of each electrode in the direction of beam axis, u_0 is the width of each non-electroded region in the direction of beam axis), $H\left(x\right)$ is the Heaviside function and ϑ is a coupling constant which will be discussed later. At an arbitrary instant of the motion, the electric potential is assumed to be linearly decreasing from $v(t)$ to 0 in $x_{i0}\le x\le x_{i1}$ whereas it is assumed to be linearly increasing from 0 to $v(t)$ in $x_{i2}\le x\le x_{i3}$. The coupling treatment given by Equation (2) is a summation of N_e terms due to the piezoelectric coupling on small fiber elements under the electric field applied. Therefore, the positions x_{i0}, x_{i1}, x_{i2} and x_{i3} change with the index *i*. As one moves from the clamped end to the free end, the index number increases. For instance, starting from the clamped end, i.e., for $i=1$:

$$x_{10}=\frac{u_e}{4},\ x_{11}=x_{10}+u_0+\frac{u_e}{2},\ x_{12}=x_{11}+\frac{u_e}{2},\ x_{13}=x_{12}+u_0+\frac{u_e}{2} \tag{5}$$

and so on for $i=1\ldots N_e$ with the increasing index number until the end of the active length. Figure 1 shows the index scheme for electrodes.

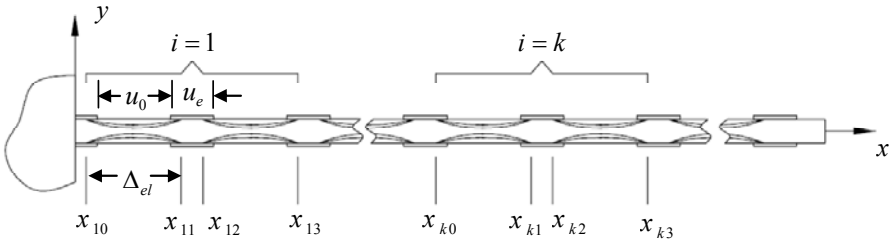

Figure 1: Geometric parameters of the piezoceramic fibers used in the coupling term (substrate is excluded.)

In Equation (2), the coupling constant is given by

$$\vartheta=-\frac{e_{33}b_{pt}\left[\left(h_d-\alpha h_p\right)^2-\left(h_c+\alpha h_p\right)^2\right]}{2\Delta_{el}} \tag{6}$$

where e_{33} is the piezoelectric constant, b_{pt} is the total width of the piezoceramic fibers, Δ_{el} is the effective electrode spacing ($\Delta_{el}=u_0+u_e/2$), h_p is the thickness of the piezoceramic fibers, h_c is the position of the bottom of the piezoceramic layer from the neutral axis and h_d is the position of the top of the piezoceramic layer from the neutral axis. Note that, the electric field is assumed to be uniform over the effective electrode spacing Δ_{el}. The form of the coupling constant given by Equation (4) is similar to the coupling constant given for a unimorph cantilever with a monolithic ceramic where the electric field is uniform and the d_{31} mode is used instead of the d_{33} mode with non-uniform electric field in reality.[8] In Equation (4), α is an empirical constant that reduces the thickness of the piezoceramic to an effective value due to non-uniform electric field. An average value of $\alpha=0.2$ is identified by matching the model predictions for a set of experiments using M8507 P1 type MFC with different substrates.

The solution of Equation (1) can be expressed as

$$w(x,t)=\sum_{r=1}^{\infty}\phi_r(x)\eta_r(t) \tag{7}$$

where $\phi_r(x)$ and $\eta_r(t)$ are the mass normalized eigenfunction and the modal response of the clamped-free beam for the *r*-th mode, respectively. For a proportionally damped system, the mass normalized eigenfunctions denoted by $\phi_r(x)$ are given by

$$\phi_r(x)=\sqrt{\frac{1}{mL}}\left[\cosh\frac{\lambda_r}{L}x-\cos\frac{\lambda_r}{L}x-\sigma_r\left(\sinh\frac{\lambda_r}{L}x-\sin\frac{\lambda_r}{L}x\right)\right] \tag{8}$$

where the dimensionless frequency numbers (λ_r) are obtained from

$$1+\cos\lambda\cosh\lambda=0 \tag{9}$$

and σ_r is expressed as

$$\sigma_r=\frac{\sinh\lambda_r-\sin\lambda_r}{\cosh\lambda_r+\cos\lambda_r} \tag{10}$$

Moreover, ω_r is the undamped natural frequency of the *r*-th mode:

$$\omega_r=\lambda_r{}^2\sqrt{\frac{YI}{mL^4}} \tag{11}$$

which is approximately the resonance frequency (for light mechanical damping) of the unimorph when the electrodes are shorted. The eigenfunctions satisfy the following orthogonality conditions:

$$\int_{x=0}^{L}m\phi_s(x)\phi_r(x)dx=\delta_{rs}\quad,\quad\int_{x=0}^{L}YI\phi_s(x)\frac{d^4\phi_r(x)}{dx^4}dx=\omega_r{}^2\delta_{rs} \tag{12}$$

Using Equation (7) in Equation (3) and applying the orthogonality conditions of the eigenfunctions gives the electromechanically coupled ordinary differential equation for the modal response of the beam as

$$\frac{d^2\eta_r(t)}{dt^2}+2\zeta_r\omega_r\frac{d\eta_r(t)}{dt}+\omega_r{}^2\eta_r(t)=-\chi_r v(t) \tag{13}$$

where

$$\chi_r=\vartheta\sum_{i=1}^{N_e}\left(\frac{\phi_r(x_{i0})-\phi_r(x_{i1})}{x_{i0}-x_{i1}}+\frac{\phi_r(x_{i2})-\phi_r(x_{i3})}{x_{i3}-x_{i2}}+\frac{d\phi_r(x)}{dx}\Big|_{x_{i0}}^{x_{i3}}\right) \tag{14}$$

and based on the proportional damping assumption, ζ_r is the modal mechanical damping ratio and it is related to the physical damping parameter through

$$\zeta_r=\frac{c_sI\omega_r}{2YI}+\frac{c_a}{2m\omega_r} \tag{15}$$

For harmonic excitation of the bimorph (i.e., $v(t)=V_0e^{j\omega t}$ where ω is the driving frequency and j is the unit imaginary number), the steady state response of Equation (13) becomes

$$\eta_r(t)=\frac{-\chi_rV_0e^{j\omega t}}{\omega_r{}^2-\omega^2+j2\zeta_r\omega_r\omega} \tag{16}$$

Physical steady state response of the beam is then obtained by substituting Equation (16) into Equation (7):

$$w(x,t)=\sum_{r=1}^{\infty}\frac{-\chi_r\phi_r(x)}{\omega_r{}^2-\omega^2+j2\zeta_r\omega_r\omega}V_0e^{j\omega t} \tag{17}$$

Hence the steady state response of the beam at its free end is

$$w(L,t)=\sum_{r=1}^{\infty}\frac{-\chi_r\phi_r(L)}{\omega_r{}^2-\omega^2+j2\zeta_r\omega_r\omega}V_0e^{j\omega t}. \tag{18}$$

2.2. Analytical and Experimental Evaluation of Unimorph Actuators

In order to validate the model given in the previous section, 12 unimorphs are fabricated by bonding an MFC actuator to commercial sheet metal substrates with epoxy. Samples are bonded in vacuum bag to

minimize variation in epoxy thickness, and air gaps. Each sample employs M8507-P1 type MFC manufactured by Smart Material Inc. which use the d_{33} mode of piezoelectricity. Three different substrate materials with different thicknesses are studied. Total overhang length of the unimorphs are approximately 80 mm and the overhang length of the active area is about $L_{act} \cong 73$ mm. Thickness and width of each piezoceramic fiber are approximately $180\,\mu m$ and $355\,\mu m$, respectively, and each epoxy layer between the fibers has a width of $51\ \mu m$. The total thickness of the active region of the MFC is $300\,\mu m$ and therefore each of the top and bottom Kapton layers in the active region is $60\,\mu m$ thick. Since the total active width is approximately 7.3 mm, each sample has approximately 18 piezoceramic fibers, yielding a total piezoceramic width of $b_{pt} = 6.4$ mm. The width of each electrode in the direction of beam length is $u_e = 97\ \mu m$ and the spacing between the electrodes is $u_0 = 410\ \mu m$. Therefore the number of electrode pairs over the beam length is $N_e \cong 72$ (therefore ~144 electrode fingers) and the effective electrode spacing is about $\Delta_{el} = 458.5\ \mu m$. M8507-P1 uses Navy II piezoceramics, for which the effective value of the piezoelectric constant is approximately $e_{33} = 19.1$ C/m^2.

The substrate materials investigated are brass, stainless-steel and aluminum. The Young's moduli for these substrate materials are taken as 105 GPa, 200 GPa and 70 GPa, respectively. The effective Young's modulus of the piezoceramic fibers is taken as 64 MPa. The epoxy type used for bonding the substrate and MFC layers is 3M DP460 and its shear strength is 4500 psi (~31 MPa). Substrate thicknesses and the average thicknesses of the epoxy layers between the substrate and the MFC layers are shown in Table 1. Note that the epoxy thickness has a variation of ±0.02mm. Epoxy thickness is an important source of uncertainty and the values listed in the table are fine tuned by comparing the analytical first natural frequency (from Eq. (12)) and the experimental natural frequency when the system is close to short circuit conditions. Note that any amplifier that is used to actuate the MFC will have its own electrical dynamics. Such effects can be significant, but here, short circuit condition is assumed. Mass per length of the MFC and the epoxy layers is estimated experimentally as 0.0123 kg/m. Total mass per length of each sample is estimated by adding this value to the mass per length of each substrate. Here, the mass densities of the brass, steel and aluminum substrates are taken as 9000 kg/m^3, 7800 kg/m^3 and 2700 kg/m^3, respectively.

Table 1: Thickness properties of each unimorph and its epoxy layer. MFC has a thickness of 0.3mm.

Sample name	Substrate	Substrate thickness [mm]	Epoxy thickness [mm]
Br 1	Brass	0.0254	0.019
Br 2	Brass	0.0508	0.010
Br 3	Brass	0.0762	0.028
Br 4	Brass	0.1016	0.033
S 1	Steel	0.0254	0.008
S 2	Steel	0.0508	0.020
S 3	Steel	0.0762	0.018
S 4	Steel	0.1016	0.059
Al 2	Aluminum	0.0508	0.015
Al 3	Aluminum	0.0762	0.018
Al 4	Aluminum	0.1016	0.019
Al 5	Aluminum	0.1270	0.042

A parametric study is conducted using the solution given in Equation (18). MFC and epoxy properties are taken as previously reported and a damping ratio of 0.005 is assumed for all modes. Solution is found for different Young's modulus and thickness ratio of substrate with respect to the constant MFC thickness of 0.3mm. The parametric study results are shown in Figure 2.

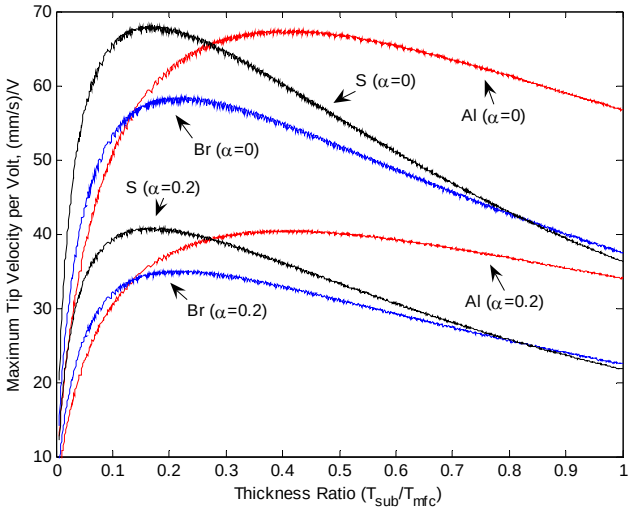

Figure 2: Analytical maximum tip velocity per volt for a range of thickness ratios. T_{mfc} is 0.3mm.

The maximum tip velocity is simply the maximum velocity achieved by the unimorph free end regardless of its frequency. As predicted, this frequency changes from sample to sample because moment of inertia and the mass per length effects the resonance frequency. The effect of empirical electric field correction factor (α) can also be seen. The velocity data is integrated (assuming zero for the constant of integration) to get the tip displacement. Similar analysis is presented for static actuation where the inertial effects simply vanish. The steady-state tip displacement for static actuation of unimorph actuators are presented in Figure 3.

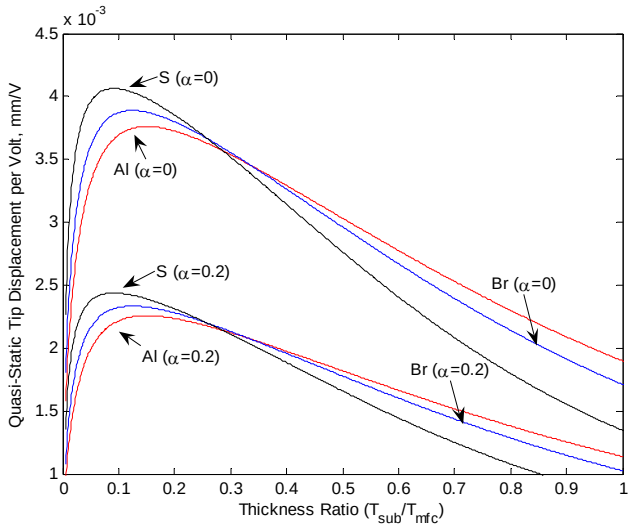

Figure 3: Static tip displacement per volt for a range of thickness ratios. T_{mfc} is 0.3mm.

The effect of the material axial stiffness shows as change in the maximum displacement (at optimum thickness ratio). The steel substrate shows the highest displacement, however at a thinner substrate when compared to a unimorph with aluminum substrate. The results given in Figure 3 is experimentally verified and modeled in the literature. [10] It must be noted that changes in α shifts the maximum displacement magnitude. This section focuses on linear dynamic actuation, so the empirical α is not found for a static (and geometrically non-linear) high-voltage actuation.

The frequency response prediction of the model is compared to the experimental case for self-excited MFC unimorphs. One of the clamped-free unimorph samples used in the experiments is shown Figure 4. A Polytec PDV-100 laser vibrometer is used to measure the tip velocity of the cantilevers, 79mm from the clamped end. The actuators are excited with a pure sine tone generated by the data acquisition system. The excitation signal is buffered by an HP 3052 unity gain amplifier. Siglab 20-42 data acquisition unit is used for data processing.

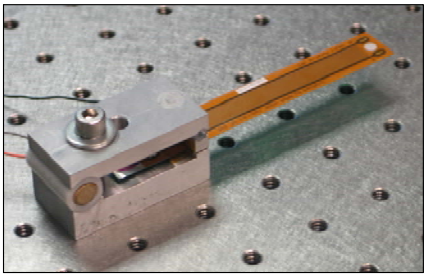

Figure 4: Clamped MFC 8507-P1 unimorph with metal substrate.

Virtual sine sweep is used for FRF measurements, where the excitation is a pure sine tone at constant frequency. The frequency is incremented only when transients are decayed from the previous frequency. Such method is utilized to avoid windowing and transients caused by more common (and faster) techniques, such as a chirp excitation. Comparison of the model predictions and the experimental measurements are presented in Figure 5.

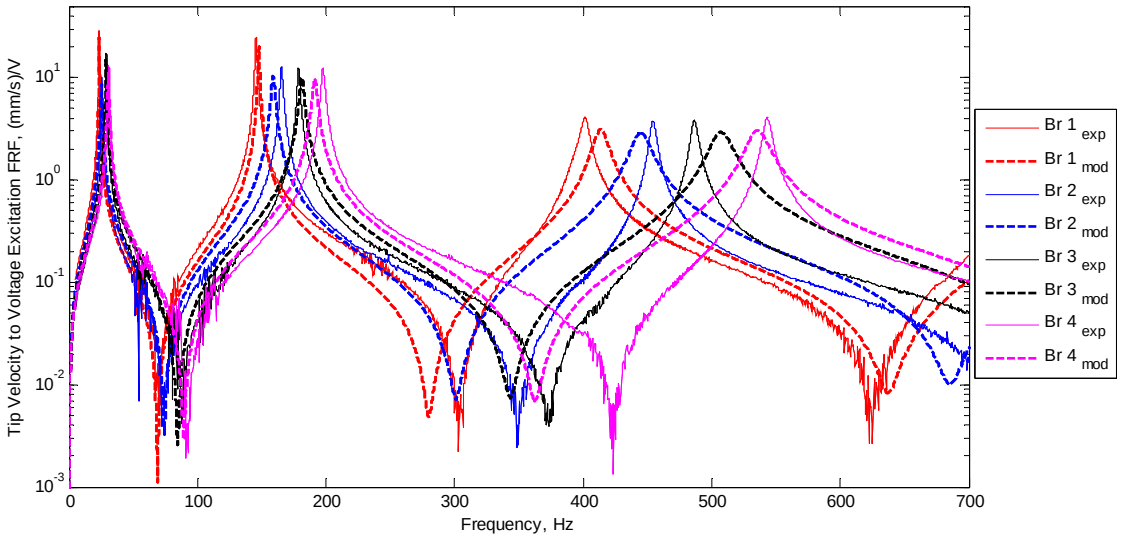

Figure 5: Tip velocity FRF comparison of experiments to model for unimorphs with brass substrates.

The FRFs presented in Figure 5 shows the unimorphs with brass substrates with four different thicknesses. It must be noted that bending stiffness used in the plot is theoretical so there is a very small mismatch between the experimental and the model prediction for the first natural frequency. The prediction for higher modes simply shift in the same direction relative to the shift observed in the first frequency. Considering the Euler-Bernoulli assumptions, this is expected since it over-predicts the natural frequencies (due to effectively stiffer assumptions of material behavior.) Table 2 shows a comparison of first three natural frequency prediction to the experimental values.

Table 2: Comparison of experimental and predicted natural frequencies in Hz.

	ω1_exp	ω1_mod	ω1 %error	ω2_exp	ω2_mod	ω2 %error	ω3_exp	ω3_mod	ω3 %error
Al 2	23.8	27.6	16.0	160.0	172.9	8.1	441.9	484.0	9.5
Al 3	31.5	32.9	4.4	194.9	206.2	5.8	530.2	577.2	8.9
Al 4	34.3	34.2	-0.4	227.3	214.3	-5.7	612.8	600.1	-2.1
Al 5	40.1	39.8	-0.6	247.4	249.6	0.9	669.3	698.7	4.4
Br 1	23.7	23.6	-0.4	145.5	147.7	1.5	401.5	413.7	3.0
Br 2	25.5	25.4	-0.6	165.2	158.9	-3.8	454.4	445.0	-2.1
Br 3	29.1	28.9	-0.7	178.6	181.2	1.4	486.4	507.3	4.3
Br 4	31.1	30.6	-1.8	197.5	191.3	-3.1	543.2	535.8	-1.4
S 1	24.7	26.3	6.5	156.6	164.7	5.1	436.9	461.2	5.6
S 2	30.7	30.5	-0.5	192.2	191.1	-0.6	521.0	535.1	2.7
S 3	32.0	31.6	-1.3	200.6	197.7	-1.4	550.4	553.7	0.6
S 4	38.1	38.1	0.0	230.5	238.4	3.4	617.9	667.4	8.0

The MFC actuated unimorph is a slender body however it includes non-linearities due to MFCs composite nature (including piezoceramic hysteresis.) The non-uniform shear layer (at the epoxy interface) is also neglected here (due to low excitation voltages) which is another source of variance of the structure from the model assumptions.

3. MFC ACTUATED THIN CIRCULAR-ARC AIRFOILS

3.1. Thin Airfoil Concepts

For simplicity of fabrication, the airfoils are designed to be variable camber plates with total thickness of 1.2% of its chord. The support system for a variable camber device intended for circulation control is shown in Figure 6. In this figure, the surface gains some camber due to the pressure loading between the supports and has a slight loss of camber on the aft end, also due to the pressure loading. The net result is an increase in circulation, although separation on the bottom side can be significant. Under-camber flow separation can be controlled with a symmetrical control surface that consists of two MFC substrates. When one substrate is strained, the other substrate serves as a flat bottom for the airfoil shape. The support system for the two surfaces must be independent, and this creates more complexity which is not addressed in this paper. For initial evaluation of the flow vectoring concept, the design in Figure 6 is modeled and tested to determine an initial estimate of control effectiveness in flow velocity of 15 m/s and Reynolds Number of 1.26E5.

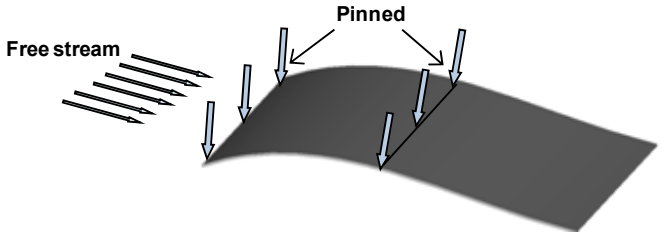

Figure 6: Flow control concept – actuated shape.

Starting with the base design given in Figure 6, three different concepts are produced. The first concept is the same design as Figure 6, with hinged supports at its leading edge (LE) and in between the LE and trailing edge (TE). In the second design, the middle support is moved to the trailing edge which is similar to a sail or a simply-supported beam. Finally, for the third concept, the airfoil is a clamped-free beam. Figure 7 shows an illustration for each concept. The label "aoa" represents the true angle of attack, "β" represents angle of the support condition, and "le_α" represents the leading edge incidence angle with the free-stream velocity.

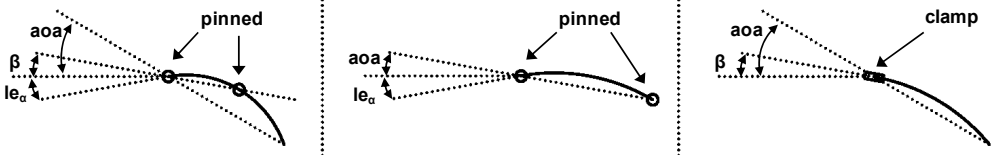

Figure 7: Three support concepts. Left: Pinned-pinned support. Middle: Sail support. Right: Clamped support.

3.2. Theoretical Aerodynamic Analysis of Airfoils and Wing Sections

The analysis of thin airfoil concepts shown in the previous section is presented here. A Matlab based program is developed to drive panel method software XFOIL[11,12], and finite element code ANSYS. The Matlab script first sends the non-aero-loaded airfoil shape to XFOIL. XFOIL calculates lift and drag coefficients and the pressure distribution. The script then takes the pressure distribution and feeds it to ANSYS which calculates a first approximation of the aero-loaded (deformed) airfoil shape. Finally, the deformed airfoil is fed back into XFOIL to calculate change in the lift and drag due to the change in pressure distribution. For XFOIL simulations, a 5% chord trailing edge gap and 1.6% turbulence level is assumed. It must be noted that XFOIL predictions above the actual stall angle should not be trusted. The airfoil is modeled as a 2D area mesh using PLANE82 high-order quadrilateral (Q8) type element in ANSYS. Approximately 1900 elements are used to ensure convergence of the finite element model for all airfoil models. The number of elements is chosen to accommodate the pressure distribution data from XFOIL.

3.3. Aerodynamic Response due to Variation in Support Locations

The analysis scheme presented in the previous section is applied to a parametric study where the two pin locations are shifted in several combinations to find the optimum pin location for generating lift when the

free-stream airflow is aligned with the pins (β=0). Pin 1 is varied from 5% chord to 60% chord downstream of the LE. Pin 2 is varied starting from 5% chord downstream of Pin 1 location to trailing edge. With these discrete scenarios, the complete range of feasible pin locations is considered. Figure 8 demonstrates the pin locations with respect to the chord of the airfoil.

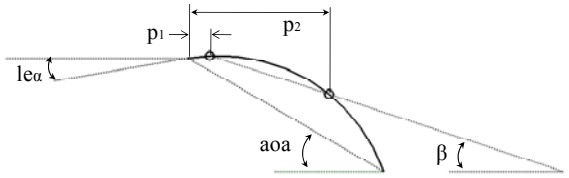

Figure 8: Illustration of the locations of Pin 1 and Pin 2.

Figure 9 shows the lift coefficient and the change in AOA for 1.2% thick circular-arc airfoil with 127mm chord. The airfoil is subjected to 700 and 1400 Volts and to 15 m/s freestream velocity. The plots present both the aero-loaded and non-loaded cases. Considering the stiffness of the airfoil, the deformation is negligible at 15 m/s. All results presented in Section 3 are for a constant β angle of zero degrees.

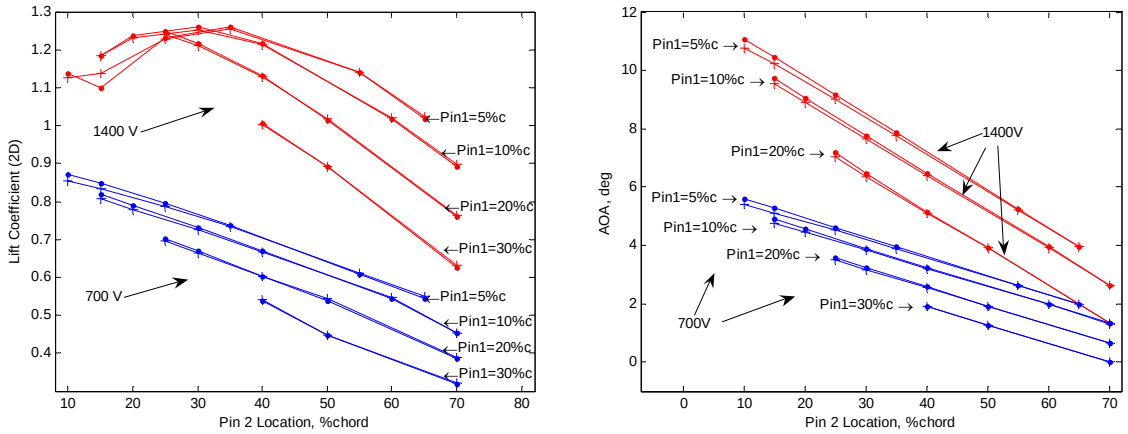

Figure 9: Theoretical (2D) results for a 1.2% thick airfoil with variable Pin1 and Pin2 locations, subjected to 700 and 1400 Volts and freestream velocity of 15 m/s. Re_{chord}=1.26E5. Left: Lift coefficient; Right: Variation of angle of attack due to pin location and voltage input.

The analysis shows that placing Pin 1 at the leading edge or 5% chord results in the best lift performance. Remainder of this section considers the cases with Pin 1 located at 5% chord. Figure 10 presents the variation of lift coefficient and AOA due to change in Pin 2 location at different actuation voltages and the freestream velocities. Both aerodynamically loaded (L) and non-loaded (NL) cases are presented.

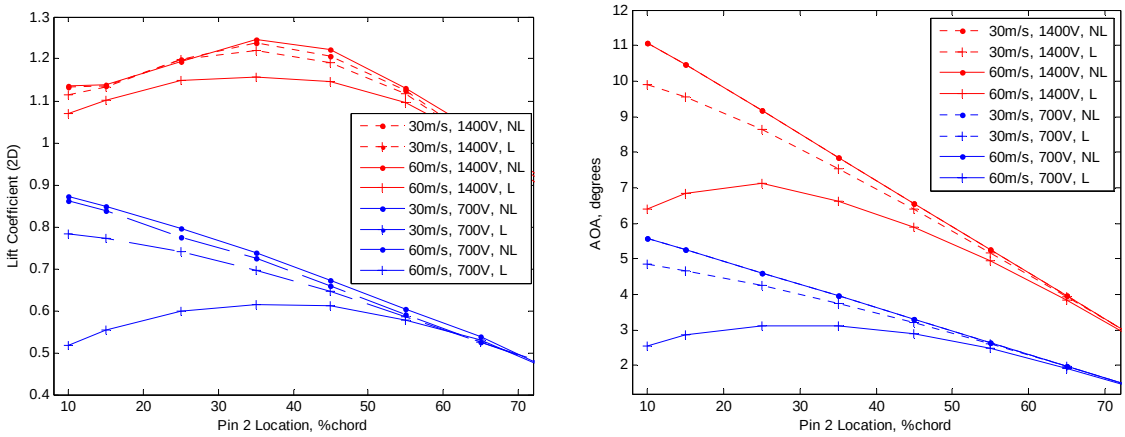

Figure 10: Theoretical (2D) results for a 1.2% thick airfoil with Pin1 at 5% chord and variable Pin2 location, subjected to 700 and 1400 Volts and freestream velocity of 30 and 60m/s. Left: Lift coefficient; Right: Variation of angle of attack due to pin location and voltage input.

The effect of higher dynamic pressures becomes clearly visible at 60 m/s between the loaded and non-loaded airfoils. At such deformations, it must be noted that the "first approximation" method used here is not

accurate since the analysis does not include any inertial effects or changes in circulation due the fluid-structure coupling. Pin 2 around 35% chord results in the optimum lift (with Pin 1 at 5% chord.)

4. THEORETICAL AND WIND TUNNEL EVALUATION OF A THIN AIRFOIL

Using the conclusions derived from the analysis presented in Section 3 and the geometric constraints, a thin MFC actuated bimorph airfoil is fabricated employing four (two on each face) MFC 8557-P1 type actuators (shown in Figure 11.) The bimorph is created by sandwiching a 25.4μm thick stainless-steel sheet and bonding the laminate under vacuum. The MFCs are aligned at the LE in the chordwise direction. A stainless-steel metal (passive material) is bonded to the TE to complete the total chord to 127mm. Four total pins (two on each end) are bonded to the airfoil at 5 and 50 percent chord from the LE.

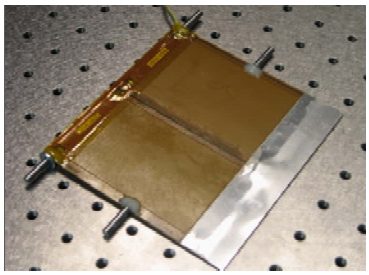

Figure 11: Prototype of variable camber airfoil with MFC actuators with 127mm chord and 133mm span.

Theoretical lift and drag coefficients for the prototype airfoil at 15m/s is given in Figure 12. Note that it is both predicted and experimentally verified that the deformation due to aerodynamic loading is negligible at this speed. Angle of the support locations (Pin1 and Pin2) is given as the independent variable. Along with the 2D viscous approximations provided by XFOIL, a vortex-lattice solution is also presented for the thin airfoil at 700 and 1400 volts. Theoretical lift curve slope for both 2D and finite span wing with aspect ratio (AR) of one is also provided in the figure for comparison.

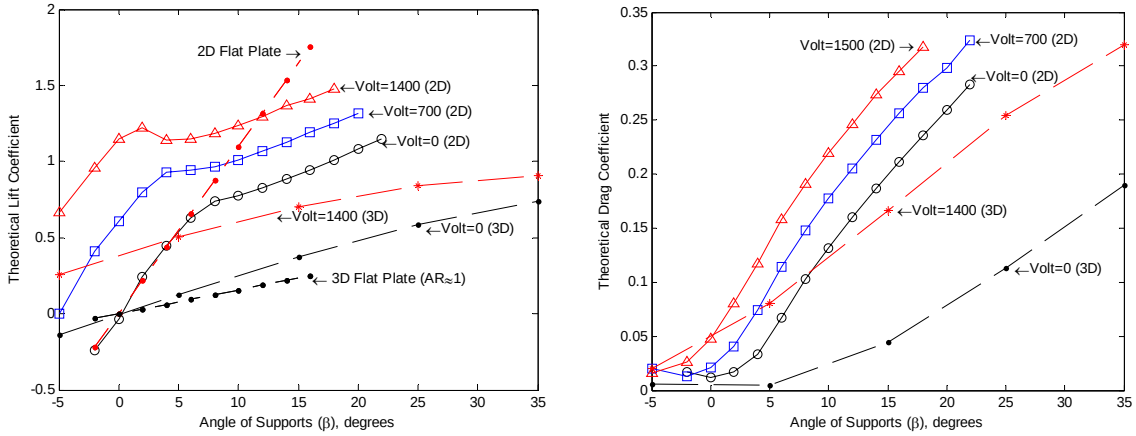

Figure 12: Theoretical predictions for a 1.2% thick airfoil supported at 5% and 50% chord subjected to 15 m/s freestream. Re_{chord}=126*10^5. Left: Lift coefficient; Right: Drag coefficient.

The difference between the 2D and the 3D airfoil is significant due to its low aspect ratio. The airfoil shown in Figure 11 is tested for lift and drag at a low speed wind tunnel with a test cross-section of 362 mm width (in direction of lift) and 137 mm height (in the spanwise direction.) Lift and drag coefficients are computed based on a wing area of S=0.0169 m^2, span of b=133 mm, chord of c=127 mm, and the measured speed. The absolute pressure of 951.2 hPa and average temperature of 23° C is measured in the test section. Using the ideal gas law, average density of air is calculated to be ρ=1.125 kg/m^3. Air velocity, u, is calculated by applying Bernoulli's equation to the Pitot-Static tube. The pressure difference across the Pitot-Static tube is recorded with the Setra 267 pressure transducer for each run. An average air velocity of 15 m/s is achieved for every run. The deformation of the airfoil is measured by two laser displacement sensors positioned in line with 5% chord and 80% chord. With the known axis of rotation of the airfoil, a third point is calculated and a circle is fitted to the three points. Such method is validated for accuracy during wind-off

conditions. Figure 13 demonstrates measured displacement and camber with the laser displacement sensors during wind-on conditions.

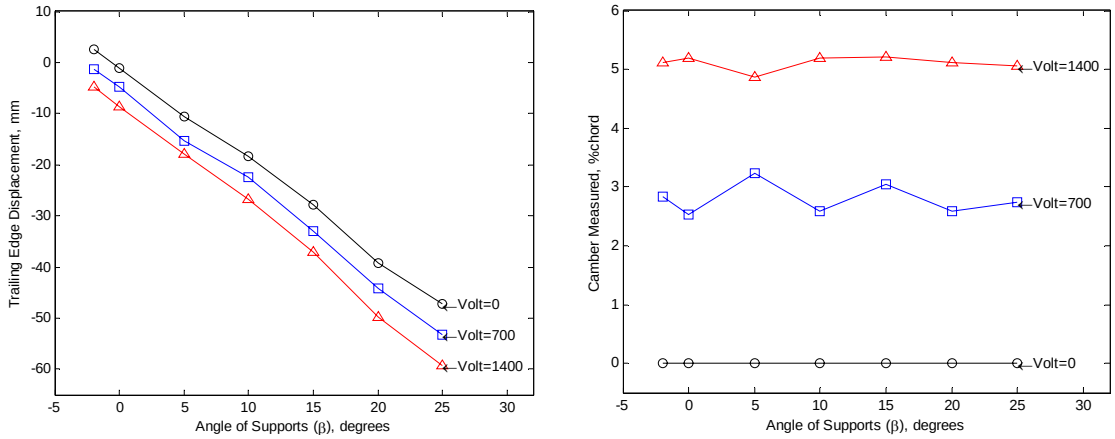

Figure 13: Geometric measurements with the lasers. Left: Displacement measured with the second laser (at 80%c) due to voltage input and the change in β. Right: Variation of effective camber under aerodynamic loads.

The effective camber values (and AOA) are derived from the displacement measurements. The measured change in AOA and camber are consistent with geometric model predictions.

Figure 14 presents the experimental results for lift and drag coefficients. Note that the angle of the pinned points (β) is given as the independent variable. The conventional angle of attack can be calculated for each voltage level using the relationships given in the figure caption.

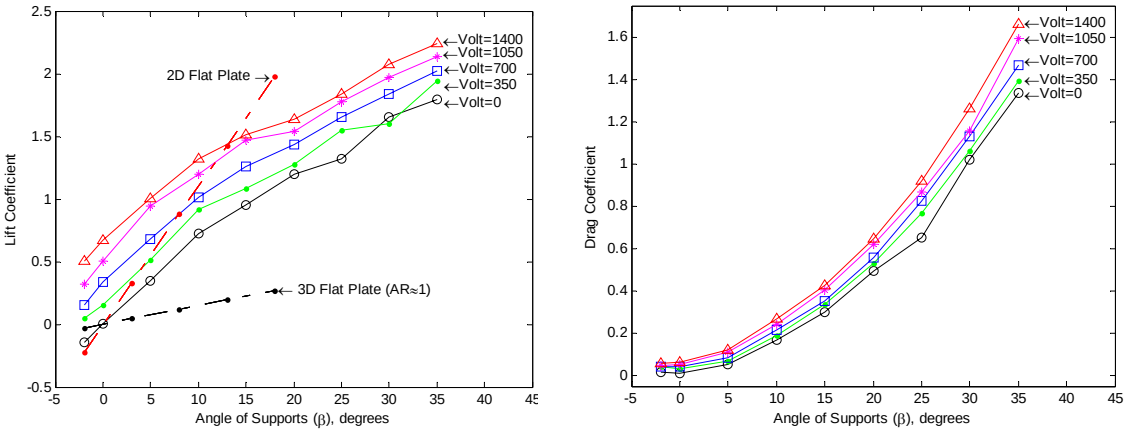

Figure 14: Aerodynamic coefficients from experiments at 15 m/s. Re_{chord}=1.26E5. Actual AOA is approximated by: $AOA_{0\text{-}Volts}=\beta$, $AOA_{700\text{-}Volts}=\beta+2.7°$, $AOA_{1400\text{-}Volts}=\beta+5.4°$. Left: Lift; Right: Drag.

The experimental lift and drag coefficients are prone to the relative errors induced by uncertainty in setting the angle β, flexibility in the mechanical beam balance system and a small amount of friction in the balance pivots. The absolute values have uncertainties due to several parameters such as air density and flow velocity measurements. [13]

The wind tunnel results show the over prediction of the 2D method, however shows the under prediction of the 3D solution from the vortex-lattice method. As reported in literature, XFOIL (2D) predicts slightly high lift coefficient and low drag coefficient when compared to experimental results. It must be noted that the turbulence in the wind tunnel is known to be higher than typical wind tunnel conditions which will change the aerodynamic performance.

It is well known to the authors from previous experiments and from literature [14,15] that the flat-plate (zero Volts) should not have high lift coefficients as observed in the experiments, and stall is expected around 10 degrees of angle of attack. The experimental values are high because of the long chord of the airfoil (127mm relative to the width of the test section of 362mm) which creates significant blockage in the test section as the angle β is increased.

The lift and drag coefficients are close to the 2D conditions (ignoring end gaps) at low β values. The test section is configured so that the root and tip of the wing section is as close to the wind tunnel walls. Experimental lift coefficient given in Figure 14 is in between the 2D and the 3D predictions, indicating that there is a significant effect due to 3D flow at the "less than perfect" boundary with the test section wall. The significant result from these plots is that there is a high gain in lift due to voltage input at zero degrees of β. The choice of support locations on the airfoil does not reduce the morphing output induced by the MFC actuation. The actuation authority does decrease slightly as the β is increased however note that non-zero values of β are not intended for the operational envelope of the airfoil. High experimental drag is observed for all AOA most likely due to the blunt LE and separation. Since these tests are primarily aimed at quantifying the thrust vectoring capability of the surface, performance in lift is considered more important than the performance in drag.

5. CONCLUSIONS AND FUTURE WORK

This study presents the modeling and wind tunnel evaluation of a variable camber airfoil with variable boundary conditions. Aerodynamic and static deflection characterization under aerodynamic loads is presented. MFCs are used to change the camber of the airfoil. Wind tunnel results show comparable effectiveness to conventional actuation systems. The concept shows adequate stiffness for flow speeds up to 30 m/s. An average lift coefficient increase of 0.5 is observed purely due to actuation voltage from 0 to 1400 Volts. The thin airfoils studied here suffered high drag.

Embedded piezoceramics in aerodynamic application provide excellent shape manipulation and also opens the door for energy harvesting during cruise conditions. Authors are currently working on a smart wing where a switched actuation/harvesting scheme is employed. The airfoil is subjected to a disturbance in the flow (in the wake of another airfoil) and energy is stored in a capacitor thru a rectifier. The stored energy is then used to suppress a known disturbance to the airfoil (going thru a gust or briefly going thru an angle where separation reduces the lift slope). The study aims to identify the feasibility of the concept, and determine aerodynamic energy input requirements for sufficient disturbance rejection.

ACKNOWLEDGMENTS

This work is supported by the G.R. Goodson Professorship endowment. The authors would like to thank colleagues at the Center for Intelligent Material Systems and Structures (CIMSS) for their support with experiments and theoretical questions.

REFERENCES

[1] Williams, R. B., "Nonlinear Mechanical and Actuation Characterization of Piezoceramic Fiber Composites," Ph.D. Dissertation, Mechanical Engineering Dept., Virginia Tech, Blacksburg, VA, March 22nd, 2004.

[2] Bilgen, O., Kochersberger, K., Diggs, E. C., Kurdila, A. J., Inman, D. J., "Morphing Wing Micro-Air-Vehicles via Macro-Fiber-Composite Actuators," AIAA-2007-1785, *48th AIAA/ASME/ASCE/AHS/ASC Structures, Structural Dynamics, and Materials Conference*, Honolulu, Hawaii, Apr. 23-26, 2007.

[3] Bilgen, O., Kochersberger, K., Diggs, E. C., Kurdila, A. J., Inman, D. J., "Morphing Wing Aerodynamic Control via Macro-Fiber-Composite Actuators in an Unmanned Aircraft," AIAA-2007-2741, *AIAA Infotech @ Aerospace Conference,* Rohnert Park, California, May 7-10, 2007.

[4] Bilgen, O., Kochersberger, K., Inman, D. J., "An Experimental and Analytical Study of a Flow Vectoring Airfoil via Macro-Fiber-Composite Actuators," Proc. of SPIE Vol. 6930, *SPIE Smart Structures & NDE 2008*, San Diego, California, 9-13 March 2008.

[5] Wilkie, W. K., Bryant, G. R., High, J. W., "Low-Cost Piezocomposite Actuator for Structural Control Applications," *SPIE 7th Annual International Symposium on Smart Structures and Materials*, Newport Beach, CA, 2000.

[6] High, J. W. and Wilkie, W. K., "Method of Fabricating NASA-Standard Macro-Fiber Composite Piezoelectric Actuators," NASA/TM-2003-212427, ARL-TR-2833.

[7] Hagood, N. W., Kindel, R., Ghandi, K., and Gaudenzi, P., "Improving Transverse Actuation using Interdigitated Surface Electrodes," SPIE Paper No. 1917-25, 1993, *North American Conference on Smart Structures and Materials*, Albuquerque, NM, pp. 341-352.

[8] Erturk, A. and Inman, D.J., 2008, A Distributed Parameter Electromechanical Model for Cantilevered Piezoelectric Energy Harvesters, *ASME Journal of Vibration and Acoustics*, **130**, 041002.

[9] Erturk, A., Bilgen O., Fontenille, M., and Inman, D.J., 2008, 'Piezoelectric energy harvesting from macro-fiber composites with an application to morphing-wing aircrafts,' *19th International Conference on Adaptive Structures and Technologies*, October 6-9, 2008, Ascona, Switzerland (submitted)

[10] Inman, D. J. and Cudney, H. H., 2000, *Structural and Machine Design Using Piezoceramic Materials: a Guide for Structural Design Engineers*, Final Report NASA Langley Grant NAG-1-1998

[11] Drela, M., "XFOIL 6.9 User Primer, XFOIL: Subsonic Airfoil Development System," Massachusetts Institute of Technology. [http://web.mit.edu/drela/Public/web/xfoil/xfoil_doc.txt]

[12] Drela, M., 'XFOIL: An Analysis and Design System for Low Reynolds Number Airfoils,' *Conference on Low Reynolds Number Airfoil Aerodynamics*, University of Notre Dame, June 1989.

[13] "AIAA Standard on Assessment of Experimental Uncertainty with Application to Wind Tunnel Testing," S-071A-1995, AIAA, New York, 1995.

[14] Hoerner, S. F., *Fluid-Dynamic Lift*, published by Mrs. Liselotte A. Hoerner, 1975.

[15] Mueller, T. J., Burns, T. F., "Experimental Studies of the Eppler 61 Airfoil at Low Reynolds Numbers," AIAA Paper 82-0345, Jan. 1982.